

Study of Ruthenium-Contamination Effect on Oxygen Reduction Activity of Platinum-based PEMFC and DMFC Cathode Catalyst

D. Kaplan^{a,b,†}, P. Tereshchuk^{c,†}, C. Olewsky^{a,†}, L. Keinan^b, O. Ben-Yehuda^b, M. Shviro^d, A. Natan^{c} and E. Peled^{a*}*

^a School of Chemistry, Faculty of Exact Sciences, Tel Aviv University, Tel Aviv, Israel, 69978

^b Nuclear Research Center - Negev, Beer-Sheva, Israel, 84190

^c Department of Physical Electronics, Tel Aviv University, Tel Aviv, Israel, 69978

^d Institute of Energy and Climate Research, IEK-14, Forschungszentrum Jülich, Jülich, Germany, 52428

Corresponding authors email addresses: peled@tauex.tau.ac.il, amirnatan@post.tau.ac.il

[†]These authors had equal contribution

Abstract

We outline a systematic experimental and theoretical study on the influence of ruthenium contamination on the oxygen reduction activity (ORR) of a Pt/C catalyst at potentials relevant to a polymer electrolyte fuel cell cathode. A commercial Pt/C catalyst was contaminated by different amounts of ruthenium, equivalent to 0.15-4 monolayers. The resulting ruthenium-contaminated Pt/C powders were characterized by Energy-Dispersive X-ray Spectroscopy (EDS), X-ray Photoelectron Spectroscopy (XPS) and Scanning Transmission Electron Microscopy (STEM) to verify ruthenium contamination. A rotating disk electrode (RDE) technique was used to study the influence of ruthenium on oxygen reduction kinetics. Density functional theory (DFT) calculations were performed to estimate the oxygen reduction activity of the platinum surface with increasing ruthenium coverage, simulating ruthenium-contaminated Pt/C. The binding energies of O and OH on the surfaces were used for activity estimations. It was found that the specific activity of the ORR at 0.85V vs RHE exhibited a pseudo-exponential decay with increased ruthenium contamination, decreasing by ~45% already at 0.15 monolayer-equivalent contamination. The results of the DFT calculations were qualitatively in line with experimental findings, verifying the effect of O and OH binding energies and the oxophilic nature of ruthenium on ORR and the

ability of the chosen approach to predict the effect of ruthenium contamination on ORR on platinum.

Keywords: ruthenium, oxygen reduction reaction, platinum, binding energies, ORR activity, DFT.

Introduction

Hydrogen-fed Polymer Electrolyte Membrane Fuel Cells (PEMFCs) and their closely related Direct Methanol Fuel Cells (DMFCs) are considered to be promising energy generators for electric vehicles (EVs), backup or off-grid power and mobile electronic devices [1, 2]. Despite intensive research over the last three decades, performance, durability and cost issues are still major obstacles to successful widespread commercialization of PEM-type FCs.

One of the reasons for cost challenges of PEMFCs and DMFCs is the fact that carbon-supported nano-size platinum (Pt/C) is used as the catalyst on the anode and cathode.

In reformat-based PEMFCs, the hydrogen stream to the anode contains CO produced by reforming or partial oxidation of hydrocarbons or alcohols and by a reverse-shift reaction of CO₂ [3,4]. In DMFCs, direct oxidation of methanol on the anode to CO₂ progresses with production of mainly CO as an intermediate. Even very low concentrations of CO (10ppm) in a reformat-based H₂ poison Pt/C catalysts [5] by strongly adsorbing on the platinum surface, hence reducing the available electrochemically active surface area and seriously inhibiting catalysis of H₂ oxidation. Likewise, in DMFCs, CO (an intermediate of methanol oxidation) is adsorbed on platinum, preventing catalysis of methanol oxidation. To solve this CO-poisoning

problem, platinum–ruthenium (PtRu) alloys are used as anode catalysts. The ruthenium component provides the oxygen-containing species needed to oxidize CO to CO₂ and release the platinum surface for further fuel oxidation [6,7].

However, PtRu catalysts were found to be prone to preferential dissolution of ruthenium [8], especially in the presence of methanol [9]. Ruthenium dissolution from the anode catalyst results in a loss of ruthenium and changes to its Pt:Ru ratio. This change leads to reduced CO tolerance and methanol oxidation activity [10] of the catalyst (for reformat-based PEMFCs and DMFCs, respectively) that will translate to higher overpotentials of the anode [11].

Ruthenium ions leaving the anode enter the Nafion membrane and cross it to deposit on the platinum cathode catalyst. Ruthenium crossover and its deposition on the cathode in DMFCs were first reported by Piela et al. of the Los Alamos Group [12]. Their pioneering work showed, with the use of XRF and CO-stripping, the presence of ruthenium in the membrane and the cathode already after MEA humidification (the so-called current-less contamination) and after operating a DMFC under various operating conditions (the so-called current-assisted contamination). Cathode contamination resulted in a voltage drop of 25mV in an H₂/air-operated fuel cell across the entire current density range. This voltage drop was ascribed to lowered catalytic activity of oxygen reduction on the Ru-contaminated cathode. Schoekel et al. reported ruthenium dissolution and deposition on the cathode already during fabrication of the MEA by decal transfer process [13]. Rapid ruthenium contamination of the cathode was recorded during early operation time (two hours) of a DMFC, and was attributed to dissolution of highly soluble ruthenium species in the anode catalyst (Johnson Matthey HiSPEC 12100). Following that, a slower contamination process was recorded, attributed to

dissolution of less soluble ruthenium oxides or ruthenium from the platinum-ruthenium alloy phase.

The negative effect of ruthenium contamination on the catalytic activity of the ORR demonstrated by Piela et al. [12], is consistent with studies of ORR kinetics on ruthenium and PtRu surfaces. Anastasijević et al. [14] studied the ORR mechanism and kinetics on a ruthenium rod. Their results clearly showed that ruthenium has poor ORR activity at potentials relevant to the PEMFC cathode. A similar conclusion can be drawn from the studies of ORR on electrodeposited ruthenium on a gold disk by Metikoš-Huković et al. [15] and ruthenium nanoparticles by Cao et al. [16]. Stamenkovic et al. [17] demonstrated the poor ORR activity of the polycrystalline PtRu (1:1) alloy electrode in comparison to the polycrystalline platinum electrode. The negative impact of ruthenium presence on ORR catalytic activity can also be seen in the case of Pt/Ru nanoparticles with exposed ruthenium on the surface [18,19].

Gancs et al. have studied the effect of platinum contamination by ruthenium on ORR catalysis [20]. In their study, different concentrations of ruthenium ions were used to contaminate commercial Pt/C by spontaneous deposition of ruthenium. With the use of different concentrations of ruthenium ions, several degrees of Ru-contamination were produced, thus enabling the study of the effect of contamination degree on CV polarization curves and ORR kinetics. Continuous suppression of H_{upd} stripping peaks with increased Ru-contamination was recorded, as well as severe decrease in ORR kinetics as evidenced by RDE polarization curves and Tafel plots. Quite close Tafel slopes were recorded for clean and Ru-contaminated Pt/C (-122 mV/dec vs 113 mV/dec respectively), indicating an identical ORR mechanism (at least at low overpotentials) for which ruthenium contamination is not a factor. Interestingly, at ruthenium coverage

of 0.18 monolayer (ML), Ru ORR kinetics reached a minimum value and a maximum overpotential of ~160 mV was recorded.

In this work we studied the influence of ruthenium contamination on ORR kinetics with the use of a commercial Pt/C catalyst (Johnson Matthey HiSPEC8000) that was Ru-contaminated. Various and precisely known amounts of ruthenium were deposited on platinum by electroless deposition at 90°C with methanol as the reducing agent. This resulted in Pt/C catalysts contaminated with different coverage levels of ruthenium. This deposition method was chosen to mimic the existing conditions in a DMFC cathode (approximated working temperature and presence of methanol which had crossed from the anode). The effect of ruthenium on ORR performance was measured by cyclic voltammetry with an RDE. We believe that this simple approach has allowed us to correlate between precisely known ruthenium contamination of Pt/C and its ORR kinetics behavior. To explain the effect of Ru contamination on the ORR activity, DFT simulations were performed for the adsorption of Ru atoms on the Pt(111) surface and their effect on the O and OH binding energies. We then followed the analysis performed by Nørksov et al. [21] to correlate the calculated binding energies with a model estimate for the ORR activity. We showed that the theoretically obtained ORR activity trends have good qualitative agreement with the experimental trend. The combined experimental and theoretical work leads to a deeper understanding of the effect of platinum contamination by a sub-monolayer to a few monolayers of ruthenium on ORR kinetics and potential losses in PEMFCs and DMFCs.

Experimental and Theoretical Methods

Catalyst synthesis

The Ru-contaminated catalysts were prepared by electroless deposition of ruthenium on commercial 50%Pt/C (HiSPEC8000, Johnson Matthey) with methanol as the reducing agent. For each catalyst, the total amount of deposited ruthenium was equivalent to 0.15-4 (0.15, 0.22, 0.6, 1, 2, 4) monolayers of ruthenium. The calculation of the required amount of ruthenium for each catalyst was made on the basis of the atomic radius of ruthenium and an approximation of spherical platinum nanoparticles with a surface area of $60 \text{ m}^2 \text{ g}_{\text{Pt}}^{-1}$ (manufacturer's data). The catalysts were named according to the amount of deposited ruthenium: 0.15ML Ru/Pt, 0.22ML Ru/Pt, 0.6ML Ru/Pt, 1ML Ru/Pt, 2ML Ru/Pt, 4ML Ru/Pt.

For the synthesis, 0.2 g of HiSPEC8000 was dispersed by vigorous magnetic stirring in an aqueous solution of 1M methanol at room temperature. The suspension was heated to $\sim 90 \text{ }^\circ\text{C}$ while being refluxed. A desired amount of $\text{RuCl}_3 \cdot 3\text{H}_2\text{O}$ was dissolved in 10 mL of 0.4 M HCl solution and added to the suspension at a rate of 1 mL every 15 minutes while the suspension temperature was maintained at $\sim 90 \text{ }^\circ\text{C}$. On completing the addition of ruthenium solution, the mixture was refluxed for an additional 30 minutes and then cooled to room temperature. The catalytic powder was recovered by centrifugation, washed with DI water until no chloride ions could be detected and dried.

Electrochemical characterization

All electrochemical experiments were performed at a controlled temperature ($25 \pm 1 \text{ }^\circ\text{C}$) with the use of a custom-made three-compartment glass cell with an Ag/AgCl/3 M KCl reference electrode in a Luggin-capillary compartment and a platinum wire as a counter

electrode. A 0.5 M H₂SO₄ solution was used as the electrolyte. All potentials are reported on the reversible–hydrogen–electrode (RHE) scale.

Measurements of the electrochemically active surface area (ECSA) of Ru/Pt/C were carried out by the Cu_{upd} stripping method [22], described in detail in our previous publication [23]. The working electrode was a 1 cm×5 cm glassy-carbon rectangle. The catalytic ink consisted of 10 mg of catalyst powder, 5 % (w/w) Nafion solution, 7.5 mL DI H₂O, 2.5 mL EtOH and XC72 that was added to obtain a concentration of 0.2-0.3 % (w/w) solids in the ink. This concentration range of solids allowed obtaining a stable ink. The Nafion volume was adjusted to be ~30 % (v/v) of the solids in the inks. The ink was dispersed for 60 minutes in an ultrasonic ice–water bath, with additional five-minute dispersion by pulse sonication (also in an ice–water bath) with the use of a horn sonicator (Heilscher UP200st). Immediately after sonication, 10 μL of the catalytic ink was applied to the lower part of the working electrode.

Nitrogen (99.999% purity) was bubbled through a 0.5 M H₂SO₄ solution for 30 minutes before electrochemical experiments and then passed over the solution during the entire procedure. Prior to ECSA measurements, the working electrodes were conditioned in order to clean their surface. A common conditioning procedure of Pt and Pt/C catalysts consists of repetitive cycling in deaerated electrolyte over a potential range of 0-1.2/1.4 volts until a stable voltammogram is obtained [24]. Cycling of Ru/Pt/C catalysts above 750mV might lead to substantial ruthenium dissolution that would result in unintended surface modification of these catalysts [9,25]. Hence, to reduce the possibility of ruthenium dissolution, the conditioning procedure of Ru/Pt/C catalysts was limited to 0-750 mV potential range [26].

For ORR measurements, a 5mm–diameter glassy–carbon RDE (Pine Instruments, USA) with $A_{\text{geo}}=0.196 \text{ cm}^2$ was used. The RDE was polished to a mirror finish with a

0.05 μm Al_2O_3 particle suspension on a moistened polishing Micro-Cloth (both from Buehler). The electrode was mounted on an interchangeable RDE holder connected to an electrode rotator (MSRX electrode rotator, Pine Instruments, USA).

The catalytic ink for ORR measurements consisted of catalyst powder, XC72 powder, 5 % (w/w) Nafion solution, DI H_2O and IPA. The Nafion volume was adjusted to 30 % (v/v) of the solids in the inks. A catalytic loading of $\sim 20 \mu\text{g}_{\text{PGM}} \text{cm}_{\text{geo}}^{-2}$ on the RDE was used and the weight of catalyst powder, DI H_2O and IPA volumes (~ 30 % (v/v) IPA [27]) were adjusted accordingly. As in the case of ECSA measurements, addition of XC72 to obtain a concentration of 0.2-0.3 % (w/w) solids in the ink enabled the preparation of a stable ink and also a uniform catalyst coating on the RDE. The ink was ultrasonically dispersed by the same procedure as the ink used for ECSA measurements, afterwards 10 μL of the ink was applied on the RDE.

Several studies have shown that a uniform catalytic film has a beneficial effect on the currents obtained during RDE ORR polarization [28,29]. We have examined different drying procedures of the ink droplet in order to obtain the most uniform film. In our laboratory environment a stationary drying procedure at room temperature with IPA environment consistently produced the most uniform catalytic films. Subsequently, this drying method was used during this research.

Nitrogen (99.999% purity) was bubbled through a 0.5 M H_2SO_4 solution for 30 minutes before electrochemical experiments and then passed over the solution during conditioning and background measurement. iR drop between the working and reference electrodes was measured and consistently found to be $\sim 4 \Omega$. Working electrodes with Ru/Pt/C were conditioned as mentioned above. Working electrodes with Pt/C were conditioned by cycling over a potential range of 0-1.2 V. For background measurements, the working electrodes were cycled for five cycles over 0-1V (for

Ru/Pt/C) or 0.025-1.2 V potential range (for Pt/C) at 20 mV s⁻¹. Background measurements were also used to measure ECSA of Pt/C by the H_{upd} stripping method [30].

Before ORR measurements, the O₂ (99.999% purity) was bubbled through the electrolyte for 30 minutes and then passed over the electrolyte during ORR polarization. The RDE potential was cycled between 1 and 0 V at 20 mV s⁻¹ while the RDE was rotated at 2500 rpm in the O₂-saturated electrolyte. The current at 0.85 V during anodic sweep polarization, after mass transport, background and iR corrections, was taken as a measure of the ORR activity, $j_k^{0.85 V}$ [31].

Physicochemical characterization

Detailed procedures of EDS and XPS measurements were described previously [32,33].

The measurements were made at ten (EDS) and four (XPS) points, respectively, in each sample of homemade catalysts and the results showed no significant inhomogeneity.

The reported results are an average of the measurements.

Transmission Electron Microscope (TEM) imaging was performed with an FEI F20 Philips-Tecnaï STEM operated at 200 kV. Samples were prepared by manually pressing the grid (200-mesh grid, EMS) against the sample powder. TEM images were used to construct particle-size distributions of the catalysts by measuring diameters of at least 80 individual particles with ImageJ software [34].

Elemental mapping was performed with the use of an FEI Titan 80-200 STEM equipped with a Cs-probe corrector (CEOS GmbH). "Z-contrast" conditions were achieved with the use of a probe semiangle of 25 mrad and an inner collection angle of the detector of 68 mrad. During STEM-EDS elemental mapping, HAADF detector and Pt L and Ru L

peaks were used. Samples were prepared by placing a drop of diluted sample on a 400-mesh carbon-coated copper grid.

Theoretical methods and computational details

Our total energy calculations were carried out with the use of DFT simulations within the Perdew-Burke-Ernzerhof generalized gradient approximation (PBE-GGA) as exchange-correlation energy functional, and the all-electron projected augmented wave (PAW) [35,36] method as implemented in the Vienna Ab initio Simulation Package (VASP) code [37,38]. For the calculations, a plane wave cut-off energy of 500 eV and k-point grids of $10 \times 10 \times 10$ and $6 \times 6 \times 1$ for the bulk and slab surface cells, respectively, were used. Geometric relaxation was considered to be complete once the atomic forces on each atom were smaller than 0.02 eV \AA^{-1} , and a total energy convergence of 10^{-6} eV for the structural energy minimization was achieved.

For the bulk fcc Pt, the calculated equilibrium lattice constant is 3.968 \AA , which is consistent with theoretical findings from the Aflow database [39] and other theoretical [40,41] and experimental [42,43] results. The calculated bulk Ru hcp parameters were $a=2.721 \text{ \AA}$ and $c=4.293 \text{ \AA}$, also in agreement with the theoretical [38,44] and experimental [45] results.

Modelling of Ru on Pt(111)

The adsorption of Ru atoms was modelled with different coverage levels (of 0.11, 0.22, 0.44, 1ML, which correspond to 1, 2, 4 and 9 atoms in the surface unit cell) on Pt(111) applying the repeated slab geometry model with a 3×3 surface unit cell and five layers in the slab separated by a vacuum region of about 25 \AA .

A single Ru ad-atom was placed at the hollow and bridge sites over Pt(111) surface as they are considered to be the most favorable positions. Then, the adsorption of

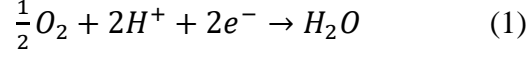
additional Ru atoms, such as 2, 4 and 9 Ru atoms, was modelled on the Pt(111) surface. In order to take into account all possible Ru geometries, as a starting point for geometrical relaxation, the Ru atoms were placed as planar and three-dimensional clusters (that is, pyramid-like configurations for Ru₄ and Ru₉) and separately diffused atoms over the Pt(111) surface. Then, geometrical optimization of the initial structures was performed, allowing all atoms to move but freezing the two bottom atomic Pt layers. Finally, the lowest energy structures were selected according to the total energies of the optimized structures.

Modelling of O and OH on Ru_nPt(111)

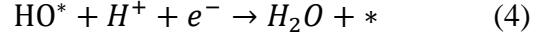
The initial structures for *m*O (*m* = 1, 2, 3, and 4) atoms on the Ru_{*n*}/Pt(111) surfaces were built on the following basis: O atoms were placed at hollow, bridge and top sites over Ru and Pt atoms. Then the systems were allowed to relax, again freezing the two bottommost Pt layers. The initial structures for *m*OH (*m* = 1, 2, 3, and 4) species on the Ru_{*n*}/Pt(111) surfaces were constructed on the basis of the optimized *m*O/Ru_{*n*}/Pt(111) structures.

Binding energies, reaction energies and activity

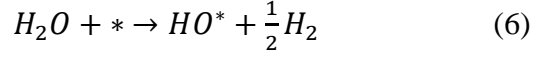
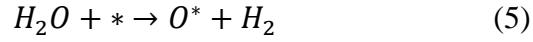
The following steps were applied for the calculations. First, the binding energies (E_b) for O atoms on Ru_{*n*}/Pt(111) surfaces were calculated as $E_b = (E(mO/Ru_nPt(111)) - E(Ru_nPt(111)) - mE(O))/m$, where the first, second and third terms are the total energies of the *m*O/Ru_{*n*}/Pt(111), Ru_{*n*}/Pt(111) and the O atoms in gas-phase, respectively. *m* is the number of O atoms in the system, the same definition for binding energy was applied also to OH (OH replacing O in all equations). For the estimation of ORR activity, we follow the approach by Nørksov et al. [21], for completeness we repeat the main principles of this approach here. The oxygen reduction reaction can be written as:



As described in [21], in the simplest way, it is possible to consider the following processes at the surface:



Here “*” implies the pure surface, and O* and OH* imply the surface with the adsorbed species. Following [21], we analyze the reaction energies for the reactions:



We assume that the hydrogen evolution reaction:



is in equilibrium for a potential $U_0 = 0$ relative to the standard hydrogen electrode. It is hence evident that the free energy change of reaction 6 is the minus of the change in reaction 4, and that the difference of the free energies of reactions 6 and 5 yields the free energy change of reaction 3. The reaction energies (ΔE_O and ΔE_{OH}) for reactions 5 and 6 for 1 and 4 O and OH on all the surfaces were computed on the basis of the total energies of the species as:

$$\Delta E_O = E(H_2) + E(O^*) - E(*) - E(H_2O) \quad (8)$$

$$\Delta E_{OH} = \frac{1}{2}E(H_2) + E(OH^*) - E(*) - E(H_2O) \quad (9)$$

In the case of m oxygen atoms (or OH species), we normalized ΔE_O and ΔE_{OH} by m . In order to account for the effect of the surrounding water molecules in the environment, the VASPSol [46,47] solvation model for water was utilized.

The free energy difference was calculated as $\Delta G = \Delta E_O/\Delta E_{OH} + \Delta ZPE - T\Delta S$, where $\Delta E_O/\Delta E_{OH}$ is the reaction energy, ΔZPE and ΔS are the changes in zero-point energies and in entropy, due to the reaction, respectively. The second and third terms in the expression are calculated by DFT and were taken by us from [21], where $\Delta ZPE - T\Delta S$ are 0.35eV for $(OH^* + \frac{1}{2}H_2)$ and 0.05eV for $(O^* + H_2)$.

For a general potential U_0 , $\Delta G_x(U_0)$ can be calculated as

$$\Delta G_0(U_0) = \Delta G_0 - 2eU_0, \quad (10)$$

$$\Delta G_1(U_0) = \Delta G_{OH} - \Delta G_0 + eU_0, \quad (11)$$

$$\Delta G_2(U_0) = -\Delta G_{OH} + eU_0, \quad (12)$$

A potential of $U_0 = 1.23V$ is assumed for the reaction of Eq. 1 to be in equilibrium. From the discussion above it is clear that ΔG_2 describes the free-energy change in reaction 4, and ΔG_1 describes the change in reaction 3, reaction 2 is partially described by ΔG_0 . In addition, the activation barrier for O_2 dissociation at the surface, E_a , was taken according to the universal relation found in [21,48]. This relation connects the reaction activation energy and the stability of the reaction intermediates, according to $E_a = 1.8*\Delta E_O - 2.89$ eV. While this relationship was established for pure surfaces, we have also extended it to our case.

The values of $\Delta G_0(U_0)$, $\Delta G_2(U_0)$, $\Delta G_1(U_0)$, and E_a can be used to calculate the different reaction-rate constants according to: $k_i \sim k_0 e^{-\frac{\Delta G_i}{k_B T}}$. We can assume that the slowest step determines the overall rate of the reaction. Hence, we [21] define the activity, A , [21, 49] by the logarithm of the rate constants, as

$$A = -\max(\Delta G_0(U_0), \Delta G_1(U_0), \Delta G_2(U_0), E_a). \quad (13)$$

A is proportional to the logarithm of the lowest reaction-rate constant.

Results and discussion

Structure and composition analysis

Weight and atomic compositions based on SEM-EDS and XPS analyses (before and after sputtering) of Ru-contaminated catalysts are shown in Table I. Both SEM-EDS and XPS show an increasing at% of ruthenium as its experimentally planned monolayer number increases, from Ru_4Pt_{96} (SEM-EDS) and Ru_7Pt_{93} (XPS) for 0.15ML Ru/Pt to

Ru₅₆Pt₄₄ (EDS) and Ru₆₅Pt₃₅ (XPS) for 4ML Ru/Pt. The only exception to this trend being 0.22ML Ru/Pt for which a lower at% of ruthenium than for 0.15ML Ru/Pt was detected by XPS analysis. We believe this anomaly is related to insufficient sensitivity of XPS at such low at% of ruthenium in both samples. All catalysts show higher at% of ruthenium on the surface compared to the situation after five minutes of sputtering (determined by XPS) and in the bulk (determined by SEM-EDS). The combined SEM-EDS and XPS results are an indication that ruthenium was deposited on platinum nanoparticles during the synthesis and not as separate nanoparticles.

Representative TEM images and size-distribution histograms (insets) of Ru-contaminated catalysts, and HiSPEC8000 are presented in Figures S1(a-i) in Supplementary Material. The average particle sizes of Ru-contaminated catalysts are similar to HiSPEC8000 up to 1ML Ru/Pt (3.7-3.9 nm) and increasing substantially to 4.5-4.6 for 2ML Ru/Pt and 4ML Ru/Pt (Table I). Several Ru/Pt catalysts show increased particle agglomeration compared to HiSPEC8000. Suspecting that the agglomeration was caused by exposure to hot reflux during the synthesis, a suspension containing HiSPEC8000 and methanol but not ruthenium salt was refluxed for the same time as during ruthenium deposition. Indeed, the resulting powder (named HiSPEC8000_M) shows significant agglomeration in TEM images (Figure S1(i) in Supplementary Material) that also manifests itself in ECSA measurements presented later.

Figures 1(a-f) show representative high-resolution STEM-EDS mappings of different Ru-contaminated single nanoparticles, with platinum colored in red and iridium in green. All examined particles of all Ru-contaminated catalysts show the presence of both ruthenium and platinum. It can be clearly seen that ruthenium was deposited on the surface of platinum nanoparticles without creating separate nanoparticles on the carbon support. In addition, with increasing amounts of added ruthenium, higher

coverage of ruthenium on platinum nanoparticles can be seen. A combination of SEM-EDS, XPS and STEM-EDS mapping measurements shows unambiguously that all Ru-contaminated catalysts have an Ru-on-Pt structure.

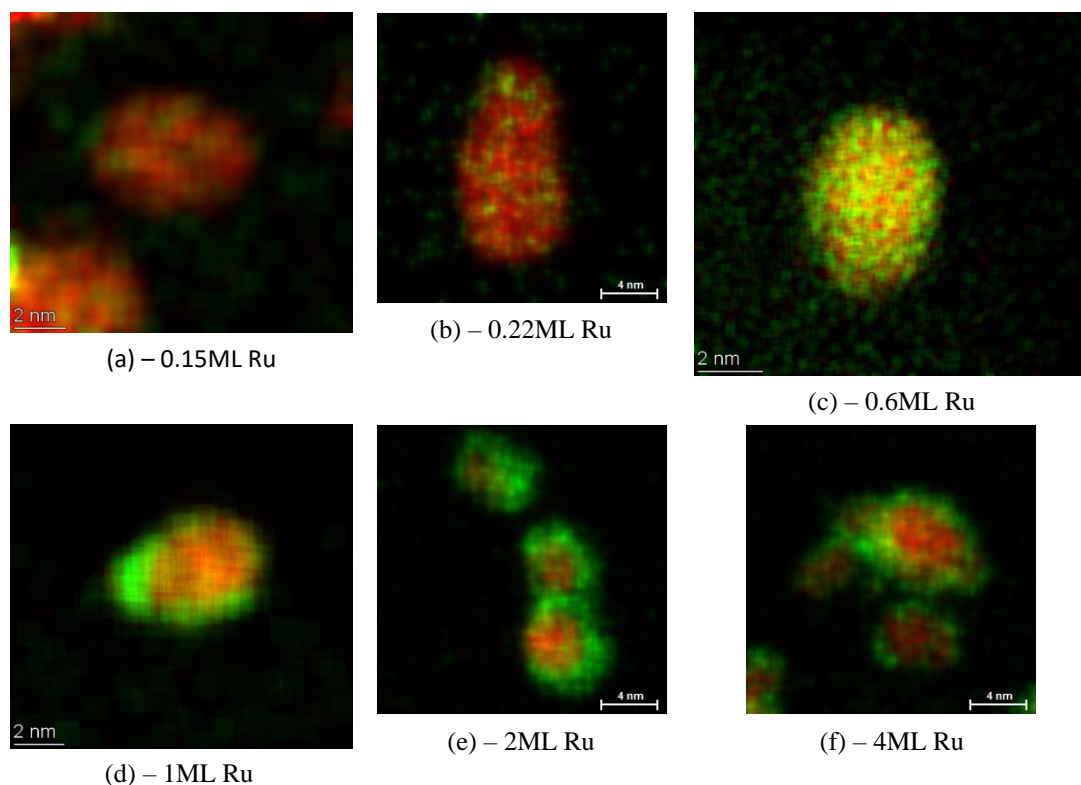


Figure 1 - HAADF-STEM elemental mapping of Ru-contaminated nanoparticles.

Platinum is marked with red and ruthenium is marked with green. (a) – 0.15ML Ru/Pt, (b) – 0.22ML Ru/Pt, (c) – 0.6ML Ru/Pt, (d) – 1ML Ru/Pt, (e) – 2ML Ru/Pt, (f) – 4ML Ru/Pt.

Table I - Physicochemical characterization results of the examined nanopowders

Nanopowder	Bulk wt% ratio	Bulk at% ratio (metals)	Surface at% ratio (metals)	Sub-surface* at% ratio (metals)	Particle size [nm]
HiSPEC8000	50%Pt/C	Pt ₁₀₀	Pt ₁₀₀	Pt ₁₀₀	3.7±1
HiSPEC8000_M	50%Pt/C	Pt ₁₀₀	Pt ₁₀₀	Pt ₁₀₀	3.9±1.2
0.15ML Ru/Pt/C	Ru _{1%} /Pt _{50%} /C	Ru ₄ /Pt ₉₆	Ru ₇ /Pt ₉₃	Ru ₅ /Pt ₉₅	3.8±1.2
0.22ML Ru/Pt/C	Ru _{1.5%} /Pt _{48%} /C	Ru ₆ /Pt ₉₄	Ru ₅ /Pt ₉₅	Ru ₃ /Pt ₉₇	3.8±1.2
0.6ML Ru/Pt/C	Ru _{4%} /Pt _{48%} /C	Ru ₁₃ /Pt ₈₇	Ru ₂₂ /Pt ₇₈	Ru ₁₄ /Pt ₈₆	3.7±0.8
1ML Ru/Pt/C	Ru _{7%} /Pt _{48%} /C	Ru ₂₁ /Pt ₇₉	Ru ₃₂ /Pt ₆₈	Ru ₁₄ /Pt ₈₆	3.9±0.8
2ML Ru/Pt/C	Ru _{17%} /Pt _{47%} /C	Ru ₃₆ /Pt ₆₄	Ru ₅₀ /Pt ₅₀	Ru ₄₁ /Pt ₅₉	4.5±1
4ML Ru/Pt/C	Ru _{26%} /Pt _{38%} /C	Ru ₅₆ /Pt ₄₄	Ru ₆₅ /Pt ₃₅	Ru ₅₆ /Pt ₄₄	4.6±1.1

*following 5min sputtering time

CV characteristics and ECSA measurement

Cyclic voltammograms of the catalysts, obtained in deaerated 0.5 M H₂SO₄, are presented in Figure 2a (Pt/C only) and Figure 2b (Ru-contaminated Pt/C). Typical platinum-characteristic features (H_{upd} stripping peaks at roughly 50-350mV and reduction peak of platinum oxides at roughly 770 mV) can be seen on the voltammogram of HiSPEC8000. The voltammogram of HiSPEC8000_M shows similar platinum features, however, it is influenced by higher agglomeration of its nanoparticles; all peaks show lower currents compared to untreated HiSPEC8000.

The voltammograms of Ru-contaminated catalysts show a gradual change as the amount of added ruthenium is increased. While H_{upd} stripping from the (110) and (100) platinum planes can be clearly seen for 0.15ML, in the cases of 0.22ML and 0.6ML Ru/Pt, the H_{upd} stripping from the (100) plane exhibits a shoulder instead of a peak.

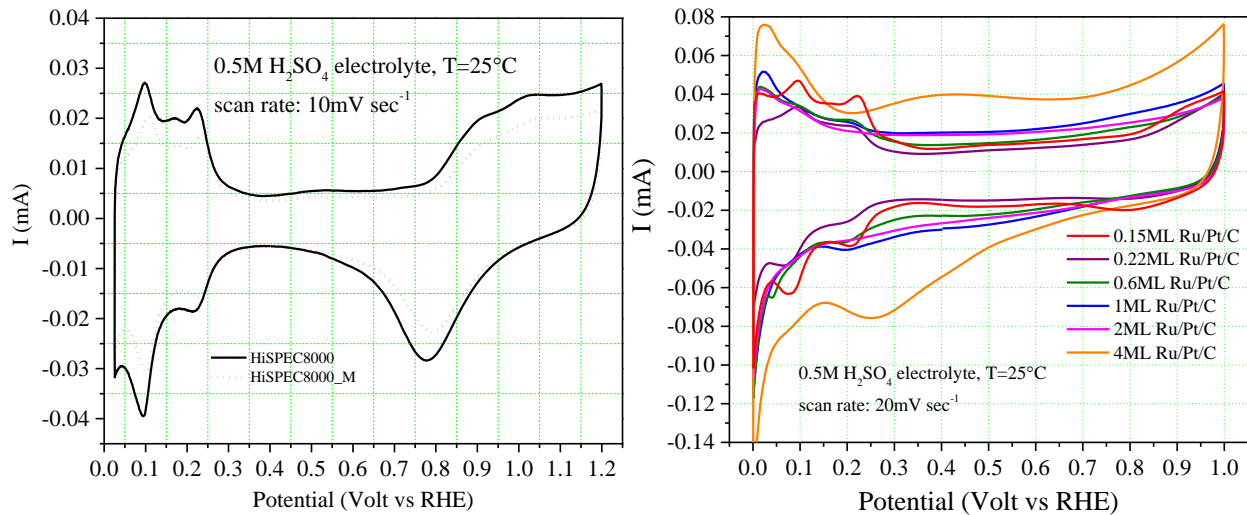


Figure 2 - Polarization voltammograms of the catalysts in deaerated 0.5 M H_2SO_4 , (a) HiSPEC8000 and HiSPEC8000_M, (b) Ru-contaminated catalysts.

Only small remnants of platinum-characteristic H_{upd} stripping region features can be seen for 1ML Ru/Pt and none can be seen for 2ML and 4ML Ru/Pt, with the latter exhibiting a ruthenium-characteristic region with a large Ru-oxide reduction peak at ~ 0.25 V (cathodic scan direction) indicating an Ru-only or highly Ru-enriched surface composition. It is clear that the gradual suppression of the platinum-characteristic H_{upd} stripping region is due to the increased ruthenium coverage of platinum. Besides changes in the H_{upd} stripping region, the "double layer" region (at roughly 350-750 mV for platinum) exhibits a gradual expansion with increasing ruthenium concentrations. This expansion originates from ruthenium oxidation/reduction [50] and high pseudo-capacitance of hydrous ruthenium oxides [51]. The observed changes in the voltammograms are consistent with previously published works [12,20,50,52] that correlated changes in voltammogram features with increased ruthenium content.

The ECSA values obtained are presented in Table II. HiSPEC8000_M shows a decreased ECSA compared to HiSPEC8000 resulting from particle agglomeration mentioned previously. ECSA values of all Ru-contaminated catalysts are lower compared to HiSPEC8000. Generally, ECSA values of nanocatalysts are affected by

particle size and their agglomeration. It appears that 1ML Ru/Pt had a lower particle agglomeration that led to a higher ECSA value compared to other Ru/Pt catalysts with similar particle sizes. On the other hand, 0.6ML Ru/Pt had higher particle agglomeration that led to lower ECSA. ECSA values of 2ML and 4ML Ru/Pt are on the lower side compared to other Ru/Pt catalysts. This was to be expected in light of the higher amount of ruthenium contamination in these catalysts that led to higher particle sizes.

Experimental study of ORR catalytic activity

ORR polarization curves of the examined catalysts are shown in Figure 3 and the obtained ORR $j_k^{0.85V}$ values are presented in Table II. Compared to Pt/C, the polarization curves of Ru-contaminated catalysts show a progressive shift of onset potentials and mixed kinetics/mass-transport regions toward more negative potentials indicating a negative effect of ruthenium contamination on ORR activity at low overpotentials. The overpotential required for reaching a mass-transport-limiting region is also negatively affected: the polarization curves of 1ML, 2ML and 4ML Ru/Pt reach a mass-transport-limiting region at substantially higher overpotentials compared to less contaminated catalysts. The appearance of a mass-transport-limiting region for 4ML Ru/Pt, despite its surface being composed of ruthenium, can be attributed to the ability of ruthenium to catalytically facilitate ORR at sufficiently high overpotentials [14,16]. Both Pt/C catalysts exhibit similar values of specific activity ($j_k^{0.85V}$) of $\sim 2.6 \text{ A m}^{-2}_{\text{Pt}}$, eliminating any possible effect of exposure to hot reflux during the synthesis and subsequent agglomeration on ORR specific activity during this research. Specific activity values of Ru-contaminated catalysts decrease with increasing amounts of ruthenium contamination. Even the smallest Ru-contamination (0.15ML Ru) leads to

massive inhibition of ORR at this potential. The largest contamination (2ML Ru and 4ML Ru) leads to practically no ORR activity, which makes both 2ML and 4ML Ru/Pt completely irrelevant as ORR catalysts for DMFCs and PEMFCs, given their cathode operating potentials.

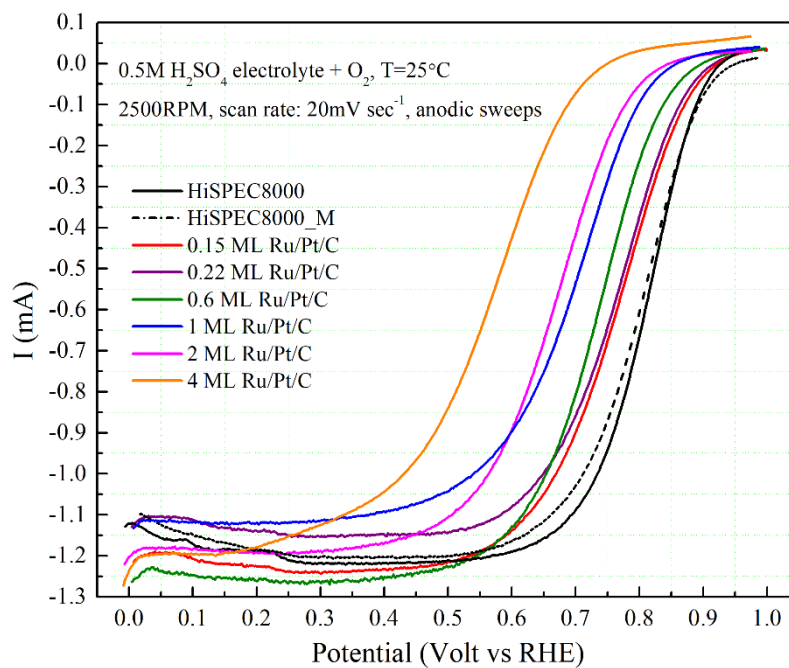


Figure 3 - RDE ORR polarization voltammograms of HiSPEC8000, HiSPEC8000_M and Ru-contaminated Pt/C catalysts.

Table II - ECSA and specific activities ($j_k^{0.85V}$) of the examined nanopowders		
Catalyst	ECSA [$\text{m}^2 \text{g}_{\text{PtRu}}^{-1}$]	$j_k^{0.85V}$ [$\text{A m}^2_{\text{PtRu}}^{-1}$]
HiSPEC8000	48±2	2.6±0.1
HiSPEC8000_M	37±1	2.6±0.1
0.15ML Ru/Pt/C	36±3	1.4±0.1
0.22ML Ru/Pt/C	38±2	1.2±0.1
0.6ML Ru/Pt/C	26±2	0.9±0.1
1ML Ru/Pt/C	42±2	0.23±0.02
2ML Ru/Pt/C	28±5	0.05±0.01
4ML Ru/Pt/C	22±2	0.013±0.002

Assuming that the decrease in ORR activity is originating from the oxophilic nature of ruthenium that covers the platinum, we used DFT calculation of the binding energies of O and OH to estimate the ORR activity on model $\text{Ru}_n/\text{Pt}(111)$ surfaces that represent Ru-contaminated Pt/C catalysts. The results of the DFT studies and their correlation to experimental results will be presented in the next sections.

Theoretical study of ORR catalytic activity

Ruthenium coverage of platinum surface

Initially, the surface energies of the clean Ru(0001) and Pt(111) surfaces were calculated. Our surface energy value for the Ru(0001) was found to be higher than that of the Pt(111) surface, that is 169 meV/A² and 95 meV/A², respectively, which is close to experimental data [53] and in agreement with other theoretical calculations from the literature [54,55].

Next, the adsorption energy of Ru atoms at the clean Pt(111) was calculated. It was found that in the lowest-energy structure, ruthenium ad-atom binds to the hollow site on the Pt(111) surface, which corresponds to the ABCA Pt stacking. In addition, it was

found that $\text{Ru}_n/\text{Pt}(111)$ structures with $n = 2, 4$ and 9 atoms, prefer planar bound structures on the $\text{Pt}(111)$ surface. A detailed description of the different geometries of $\text{Ru}_n/\text{Pt}(111)$ ($n = 1, 2, 4, 9$ atoms) and their adsorption energies can be found in Supplementary Material in Figures S2 and S3. It is known from the literature that there is formation of Ru monatomic layers at low coverages [56] and bilayer islands and three-dimensional clusters at higher levels of coverage [56-57]. Our surface cell was slightly too small to show the effect of multilayer formation and hence in our simulations, the ruthenium atoms typically tended to form a monolayer. A Bader charge analysis reveals that the Ru atoms tend to give some of their electrons to the Pt surface. For $\text{Ru}_1/\text{Pt}(111)$ we found that the Ru atom had a Bader charge of $+0.34e$. For the $\text{Ru}_2/\text{Pt}(111)$, the charge was $+0.29e$ per Ru atom (total of $+0.57e$), for $\text{Ru}_4/\text{Pt}(111)$, the charge was $+0.21e$ per Ru atom (total of $+0.85$), and for full coverage of $\text{Ru}_9/\text{Pt}(111)$ we found a charge of $+0.11e$ per Ru atom (total of $+1.01e$ for the Ru monolayer).

O binding on $\text{Ru}_n/\text{Pt}(111)$ surface

As found previously [58-61], and also supported by us, the O atom has a greater tendency to bind on hollow sites on both the pristine $\text{Pt}(111)$ and $\text{Ru}(0001)$ surfaces. On the $\text{Ru}_n/\text{Pt}(111)$ surfaces it was found that O atoms generally tend to bind on the Ru atoms, which can be explained by the stronger binding of O atom on the $\text{Ru}(0001)$ (with calculated binding energy, E_b , of -5.97 eV) compared with that of binding on the $\text{Pt}(111)$ (calculated E_b of -4.25 eV). The lowest energy structures for $m\text{O}$ on $\text{Ru}_n/\text{Pt}(111)$ surfaces are presented in Figure 4.

Since we examine the thermodynamic limit of lowest energy structures, the binding energy of a single oxygen atom will not be much affected by the Ru-atom coverage level, even if the coverage is one Ru atom per million Pt surface atoms, the oxygen

would still tend to bind to the Ru atom. To fully account for an actual scenario, one needs to build a kinetic simulation which takes into account the adsorption on alternative surface sites. Here we use an alternative approach of saturating the surface with oxygen atoms. At some point, the next oxygen atom cannot bind to the Ru atom(s) and binds instead to a Pt surface atom, hence showing Ru-coverage-dependent behavior.

On the Ru₁/Pt(111) one O atom binds Ru on-top site with a bond length (R_{O-Ru}) of 1.67 Å, and then the second and the third O atoms tend to bind on this single Ru atom and also to Pt, with R_{O-Ru} of 1.77/1.80 Å and R_{O-Pt} of 2.10/2.04 Å for 2O/3O atoms, respectively. The fourth O atom binds to the hollow site over Pt(111) with R_{O-Pt} of 2.04-2.05 Å.

A Bader charge [62,63] analysis of *m*O on the Ru₁/Pt(111) surface was performed. At 1O/Ru₁/Pt(111), the Ru atom has a charge of +0.95 e and the charge of the O atom is -0.60 e , while at 2O/Ru₁/Pt(111), the charge redistribution (transfer) between Ru and O atoms is enhanced, i.e., the Ru atom has a larger positive charge, namely +1.27 e and the charges on O atoms are -0.68 e and -0.61 e . Following the trend, the charge on the Ru atom is increased to +1.60 e at 3O/Ru₁/Pt(111) and the charges on the O atoms are -0.61 e , -0.68 e , -0.68 e . Because of the saturation by O atoms, the fourth O atom in the 4O/Ru₁/Pt(111) has a charge of -0.65 e and is adsorbed at a hollow site of the Pt surface (not near the Ru atom).

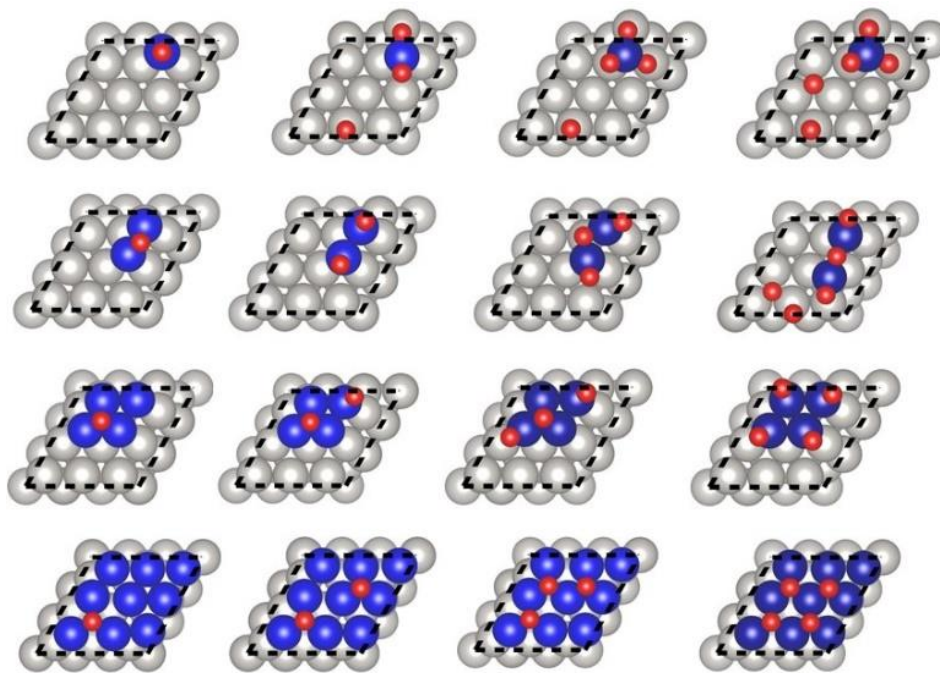


Figure 4 - The lowest energy structures for $m\text{O}$ ($m = 1-4$) atoms bound on $\text{Ru}_n\text{Pt}(111)$ ($n = 1, 2, 4, 9$) surfaces. Pt atoms are shown in gray, Ru atoms are shown in blue and oxygen atoms are shown in red.

For the adsorption of O atoms on the $\text{Ru}_n/\text{Pt}(111)$ ($n=2$ and 4), the following trend was observed. The more Ru atoms on the Pt(111) surface, and, hence, the more place for adsorption, the more O atoms tend to occupy the Ru bridge and then hollow Ru sites. On the $\text{Ru}_2/\text{Pt}(111)$, O atoms bind on bridge and top sites for 1O and 2O atoms with $R_{\text{O-Ru}}$ of 1.89 Å and 1.67 Å, respectively. For 3O and 4O there is a mixture of two on-top and one O-bridge site bindings on Ru, the fourth O, for 4O, binds on a hollow site over Pt(111). One of O in 4O/ $\text{Ru}_2/\text{Pt}(111)$ is on a Pt hollow site. One of the O atoms in the 1O, 2O and 3O structures on the $\text{Ru}_4/\text{Pt}(111)$ is on a Ru hollow site, while the remaining O atoms are on-top Ru sites. For 4O/ $\text{Ru}_4/\text{Pt}(111)$ all O atoms bind to on-top Ru sites. The most energetically favorable binding sites for O are the hollow sites over Ru atoms for the case of $\text{Ru}_9/\text{Pt}(111)$ with $R_{\text{O-Ru}}$ of 1.96-2.06 Å.

OH binding on Ru_n/Pt(111) surfaces

The binding of OH species to the Ru_n/Pt(111) surfaces follows trends similar to that of the binding of O atoms, namely, OH species first bind to Ru atoms and occupy all possible sites on these atoms. However, in addition, OH can also form hydrogen bonds with either other OH or surface atoms. This can further stabilize some surface-adsorbed structures. The structures for the OH binding on the Ru_n/Pt(111) are presented in Figure S4 in Supplementary Material.

Binding energies for O and OH

The binding energies (E_b) for m O and m OH ($m = 1-4$) species on the clean Pt(111) and Ru(0001) surfaces, and on the Ru_n/Pt(111) ($n = 1,2,4,9$) surfaces, are presented in Figure 5. For the pristine surfaces it was found that the E_b of a single O atom on Pt(111) is weaker than on Ru(0001): -4.25 eV and -5.97 eV, respectively, which is consistent with literature results [56,59,64].

For the Ru_n/Pt(111) surfaces it is found that the oxygen binding energy, E_b , decreases with the number of adsorbed oxygen atoms. This trend is especially strong for the Ru₁/Pt(111) (E_b decreases from -5.86 eV for a single oxygen to -4.87 eV with four oxygens) and Ru₂/Pt(111) (from -6.21 to -5.10 eV) surfaces. This can be explained by the saturation of Ru sites which forces some of the oxygen atoms to be adsorbed on Pt atoms and not on the Ru atoms. This decrease in E_b still exists but is less prominent for the case of Ru₉/Pt(111) (E_b changes from -6.35 to -5.92 eV), where all the O atoms are uniformly distributed above the full-coverage Ru monolayer. Here, and also on the clean Pt(111) and Ru(0001) surfaces, another mechanism, of electrostatic repulsion between the adsorbed oxygen atoms, can explain the smaller decrease in the binding energy.

The E_b for mO atoms on the $Ru_n/Pt(111)$ is stronger than on $Pt(111)$ and closer to the E_b of $Ru(0001)$. This finding can be related to the strain and ligand effects on the $Ru_n/Pt(111)$ systems, that play an important role in controlling the surface reactivity [65], and is in agreement with the experimentally known oxophilic nature of ruthenium (compared to platinum). For $Ru_4/Pt(111)$, the binding energy, E_b , for 4O atoms approaches that of $Ru(0001)$ because all the oxygen atoms tend to adsorb on Ru sites. However, it is statistically possible that one or more of the O atoms can also bind to Pt atoms at a higher energy state. We therefore considered an additional higher energy structure, defined as $Ru_4/Pt(111)^*$, where one of the O atoms is adsorbed on the Pt surface and not on the Ru_4 cluster.

The E_b for OH species shows a trend similar to that of the E_b of O atoms, except for the case of $4OH/Ru_n/Pt(111)$, in which we found a stronger binding of $4OH$ relative to $3OH$ on most surfaces. This can be explained by the contribution of the hydrogen bonds between the hydrogen and Pt/Ru atoms on these surfaces.

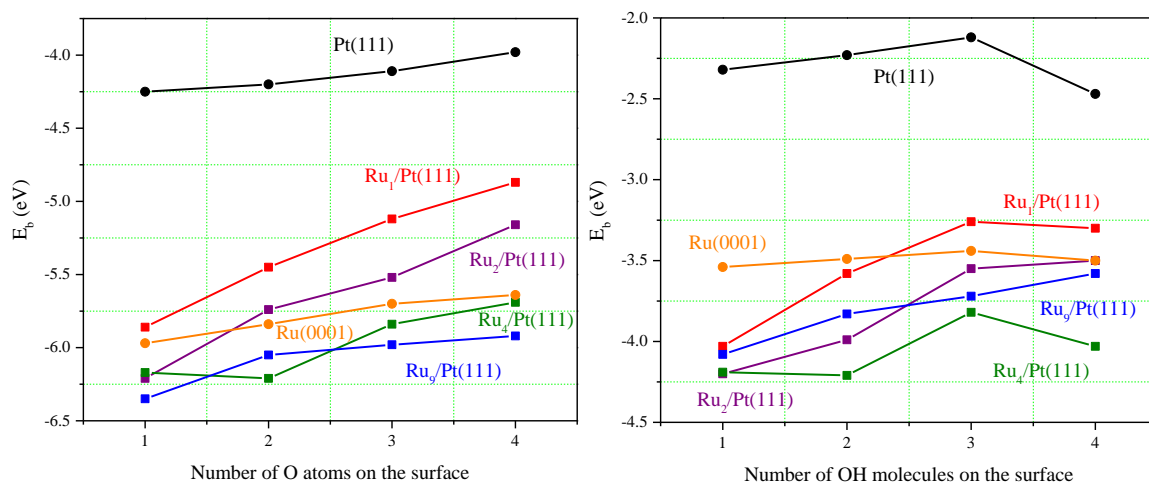


Figure 5 - Binding energies (E_b) for mO atoms and mOH species ($m = 1-4$) on the $Ru_n/Pt(111)$ ($n = 1, 2, 4, 9$). Here, the black, orange, red, violet, green and blue lines correspond to the cases of $Pt(111)$, $Ru(0001)$, $Ru_1Pt(111)$, $Ru_2Pt(111)$, $Ru_4Pt(111)$ and $Ru_9Pt(111)$, respectively.

Estimated ORR activity of Ru_n/Pt(111) surfaces

The ORR activity was estimated by calculating $\Delta G_0(U_0)$, $\Delta G_2(U_0)$, and $\Delta G_1(U_0)$, and estimating the minimum as described in Equation 13. Results for single O/OH adsorption and for 4O/OH adsorption are shown in Tables SI and SII in Supplementary Material. The results for the calculated activity as a function of ΔE_O and ΔE_{OH} for the case of 4O atoms and 4OH species are shown in Figure 6. This figure also includes an estimated activity for the higher energy structure Ru₄/Pt(111)* for which 3O/OH species are adsorbed on Ru sites and one O/OH is adsorbed on Pt(111). This structure can be considered as more representative of a real-world situation compared to the lowest energy case where all species are adsorbed on the Ru atoms and none on the platinum. It can be seen that for both single O/OH (Fig. S5 in Supplementary Material) and 4O/OH (Figure 6 and Figure S6 in Supplementary Material) the addition of Ru atoms is followed by a decrease in ΔE_O and ΔE_{OH} (i.e., increased binding of O and OH) that leads to a decrease in ORR activity. It is also evident from Figures S5 and S6, that the effect of Ru coverage on ΔE_O , ΔE_{OH} and the estimated ORR activity is more pronounced for the case of 4O/OH. The reason for this is that a single O/OH will always have an available Ru site to adsorb on, while in the case of 4O/OH, the Ru sites become saturated at low Ru coverages.

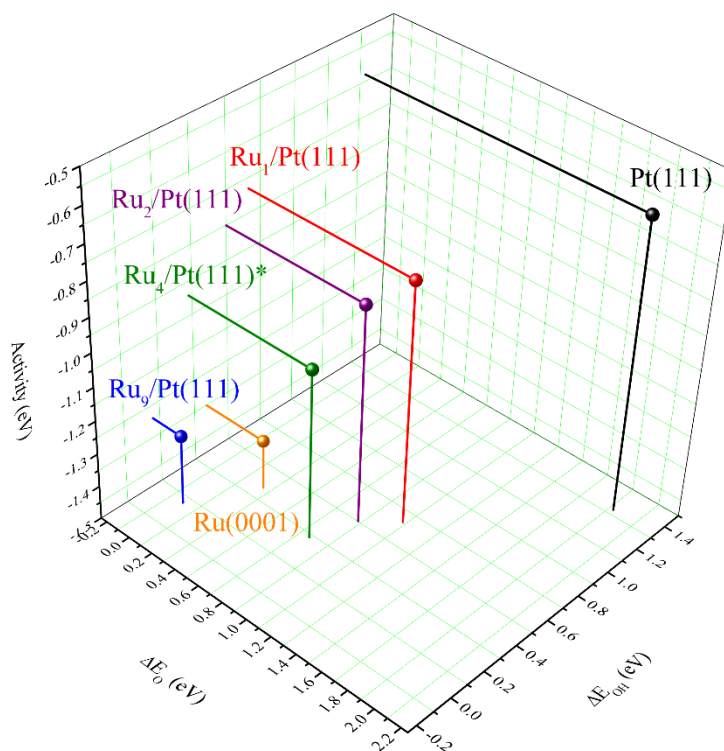


Figure 6 - Estimated ORR activity A (according to Eq. 6) as a function of ΔE_O and ΔE_{OH} . These data are for the adsorption of four oxygen atoms and an OH species. Here, the presented data correspond to the lowest energy structures of Pt(111), Ru₁/Pt(111), Ru₂/Pt(111), Ru₉/Pt(111), Ru(0001), and a higher-energy structure of Ru₄/Pt(111), Ru₄/Pt(111)*, which represents a more probable real-world structure. Figure S6 in Supplementary Material contains the data for the lowest-energy structure of Ru₄/Pt(111).

Analysis of ruthenium effect on ORR

The DFT calculations presented above clearly show that indeed the oxophilic nature of ruthenium (compared to platinum), that manifests itself in increased O and OH binding, is the root cause of the inferior ruthenium ORR activity at potentials relevant to PEMFC. According to the Sabatier principle, too-strong binding of O and OH on ruthenium (compared to platinum) reduces the possibility of O and OH hydrogenation that is needed in order to complete O₂ reduction to H₂O. Moreover, because of its

oxophilic nature, ruthenium is oxidized at much lower potentials compared to platinum. Hence, at PEM-cathode operating potentials ruthenium is oxidized, cannot adsorb O₂ molecules and facilitate their reduction. Besides being effectively ORR-inactive, ruthenium deposited on platinum (as in the case of Ru-contaminated platinum studied here) masks three platinum atoms, preventing them from adsorbing O₂ molecules and effectively reducing the available platinum sites (i.e., available surface area) for ORR. Figures 7a and 7b exhibit the estimated and experimental ORR activity as a function of Ru coverage. It can be seen that for both theoretical and experimental methods the addition of Ru atoms leads to a decrease in ORR activity. Although expressed in different units, qualitatively similar trends can be seen in both figures, validating the use of O and OH binding energies for the estimation of ORR activity.

In Figure 7b it can be seen that the deposition of a 0.15 equivalent monolayer of ruthenium (0.15ML Ru/Pt) resulted in a decrease of ~45% of ORR activity. Given the explanation presented above, attributing the decrease of ORR activity to the coverage of three platinum atoms by a single ORR-inactive ruthenium atom, and the clear presence of platinum features on the voltammogram of 0.15ML Ru/Pt, the massive decrease in ORR activity is quite surprising, i.e., a less severe decrease in ORR activity can be expected. Moreover, additional deposition of ruthenium, up to 0.22 and 0.6 equivalent monolayers (0.22ML Ru/Pt and 0.6ML Ru/Pt) hasn't resulted in such a drastic decrease in ORR activity; the ORR activity decreased by ~20% when the equivalent monolayer was increased from 0.15 to 0.22 and from 0.22 to 0.6. Further deposition of ruthenium to 1, 2 and 4 equivalent monolayers (1ML Ru/Pt, 2ML Ru/Pt and 4ML Ru/Pt) leads to a saturation in ORR activity decrease. A question arises regarding the reason for this behavior of ORR activity, that appears to exhibit an exponential-like decay with increased ruthenium coverage (as demonstrated by

exponential decay fit in Figure 7b). In order to answer this question, it is necessary to examine the mechanism of O₂ reduction on a platinum surface and the preferred deposition of Ru sub-monolayers on Pt surfaces.

Although ORR is a multistep reaction with a quite complex mechanism that is still somewhat in debate [21,66,67], the breaking of an O–O bond (i.e., O₂ dissociation) and the formation of O–H bonds [66] involving a four-electron process must occur in order to achieve a complete reduction of O₂. Among multiple possible configurations for O₂ adsorption on a platinum surface, adsorption on two adjacent platinum sites (the so-called bridge side-on) is generally favored for the promotion of O₂ dissociation [68,69]. As mentioned above, ruthenium adsorbed on platinum masks three platinum sites, preventing those sites from adsorbing O₂ in any configuration. We shall name this type of platinum deactivation a direct deactivation. Nine platinum sites surrounding the masked three platinum sites lose some of their potential neighbors for bridge side-on adsorption. This may lead to increased probability for O₂ adsorption in a less favorable configuration for O₂ dissociation and thus negatively affecting ORR kinetics. We shall name this type of deactivation an indirect deactivation. Hence, one ruthenium atom has the potential to deactivate to some degree, **twelve** atoms of platinum and not only three atoms. We believe this to be the reason for the massive decrease in the ORR activity for 0.15ML Ru/Pt.

We shall now turn our attention to the deposition of ruthenium sub-monolayers on platinum surfaces. As was mentioned previously, ruthenium deposition on platinum has a tendency to create monolayer clusters at low coverages and bilayer islands and three-dimensional clusters at higher coverages (Volmer–Weber growth). It is likely that for 0.22 and 0.6 equivalent monolayers such islands will be formed, hence effectively reducing the number of platinum sites deactivated by each ruthenium atom and

reducing the decrease rate in ORR activity with increased ruthenium deposition. Additional reduction of deactivated platinum sites for each ruthenium atom (and subsequent reduction in ORR activity decrease rate) is expected as a result of the overlap between the deactivated platinum sites. It is reasonable to assume that such overlap will occur at sufficiently high ruthenium coverage and will grow as ruthenium coverage is increased until the ORR activity will reach a plateau value that is similar to the ORR activity of ruthenium. We believe that the proposal described above provides an explanation for the observed exponential-like decay of ORR activity on Ru-contaminated Pt/C.

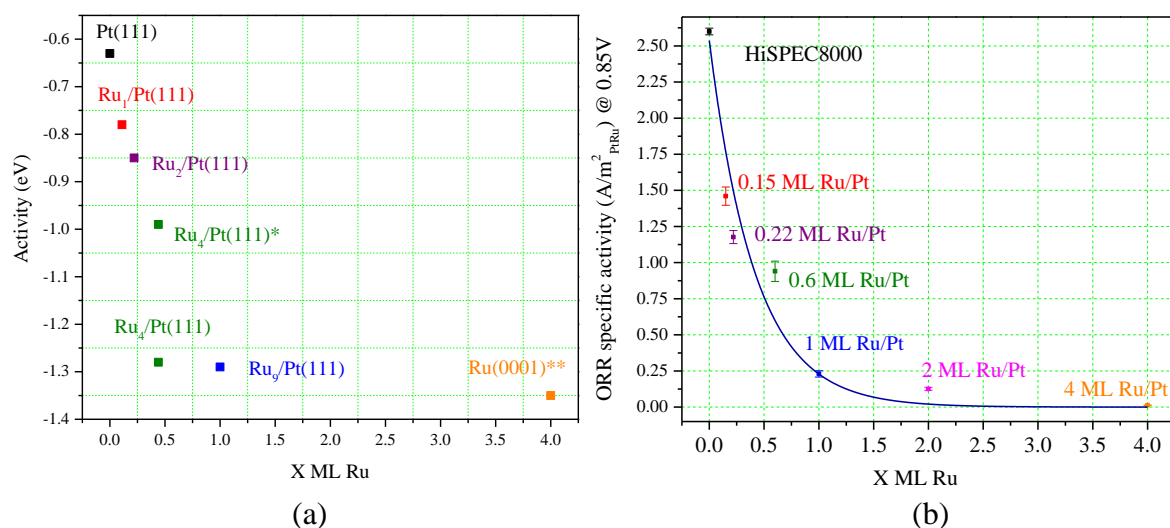


Figure 7 - (a) Estimated ORR activity according to Equation 6 and (b) experimentally measured activity as a function of ruthenium coverage. An exponential decay fit (blue line) is used to demonstrate the exponential-like decay of experimentally measured activity with increasing ruthenium coverage. Estimated activities were calculated for the lowest energy structures, except for Ru₄/Pt(111)*, for which both the lowest-energy and a higher-energy and more realistic structure were used (see explanation in the text). **The Ru(0001) surface was used to simulate the case of a 4ML Ru coverage.

Implications of ruthenium contamination on the performance of reformat-based PEMFCs and DMFCs

Even though RDE ORR experiments cannot precisely predict an FC cathode polarization, they can be used to obtain a first-order approximation of it. Hence, the RDE ORR polarization data obtained during this research can be used to assess the overpotential penalty of an FC cathode originating from ruthenium contamination.

To assess the added overpotential, we shall look at Figure 8, which presents mass-transport, background and iR-corrected Tafel plots for HiSPEC8000 and 0.15ML Ru/Pt. The latter was chosen because of the similarity of its ruthenium content to ruthenium contamination found by Piela et al. [12]. In order to approximate the overpotential, we compare the potentials of both RDEs at the same current densities that polarize the RDEs to typical potential ranges of DMFC and PEMFC cathodes during FC operation. The catalyst loadings on RDEs for both catalysts were similar, $\sim 20 \mu\text{g}_{\text{PGM}} \text{cm}_{\text{geo}}^{-2}$, hence any overpotential for 0.15ML Ru/Pt can be associated with ruthenium contamination.

Looking at the potential range typical to operating DMFC cathode, $\sim 0.8\text{V}$ [70,71,72,73], it can be seen that the approximated overpotential penalty (marked as η_{Ru} at Figure 8) for 0.15ML Ru/Pt is roughly 45mV. Assuming a cell voltage of 0.45V during DMFC operation, this penalty will translate to roughly 10% decrease in power density. The overpotential penalty grows to roughly 75 mV over a potential range typical to an operating PEMFC cathode, $\sim 0.65\text{V}$. Taking into account the small overpotential of a PEMFC anode and assuming a cell voltage of 0.6V during operation, we can approximate the penalty in power density at slightly more than 10%.

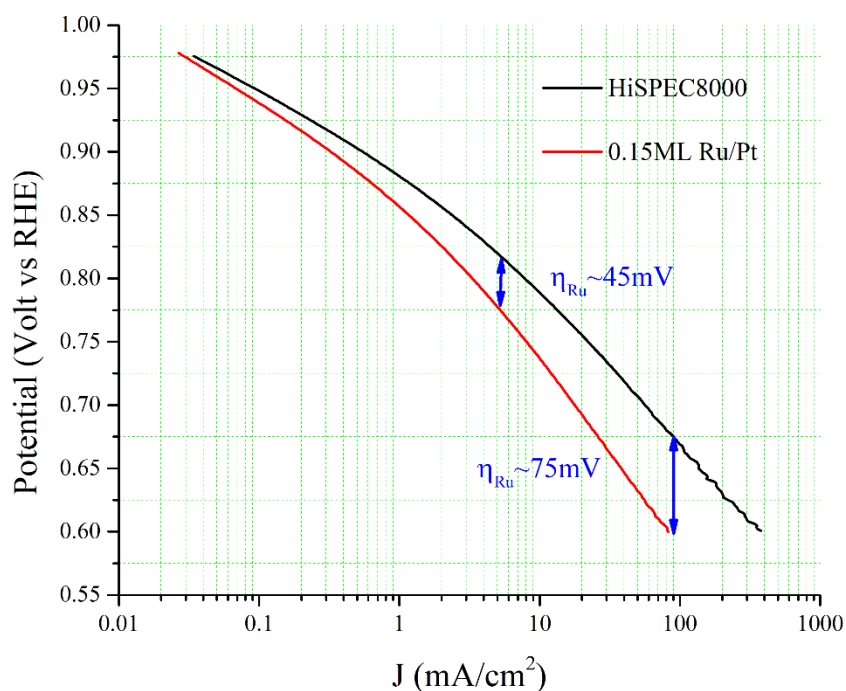


Figure 8 - Tafel plots for oxygen reduction on HiSPEC8000 and 0.15ML Ru/Pt. The plots were produced with the use of RDE ORR polarization voltammograms shown in Figure 3 following mass-transport, background and iR corrections.

Conclusions

In this work we studied the effect of ruthenium contamination on ORR on platinum, focusing on the implications on PEMFC and DMFC cathode-relevant potentials. To obtain our objective, a commercial 50%Pt/C catalyst was contaminated by precisely known amounts of ruthenium. The contamination range varied from relatively low contamination, equivalent to 0.15ML of ruthenium, to severe contamination, equivalent to 4ML of ruthenium.

The contaminated catalysts were examined with the use of physico-chemical methods to verify and quantify ruthenium contamination. It was found that ruthenium was

deposited on the surface of platinum nanoparticles in a core-shell-like structure without creating separate ruthenium nanoparticles on the carbon support.

H_{upd} -stripping region analysis showed a gradual suppression of the platinum-characteristic hydrogen region that was correlated with increased ruthenium coverage of the platinum. While H_{upd} -stripping peaks from (110) and (100) platinum planes could be seen for 0.15ML Ru/Pt, only small remnants of platinum-characteristic features could be seen for 1ML Ru/Pt, while higher ruthenium contamination showed ruthenium-characteristic features.

RDE ORR polarization showed the negative effect of ruthenium on ORR at potentials relevant to the PEMFC/DMFC cathode, exhibiting a progressive shift of onset potentials and mixed-kinetics/mass-transport regions toward more negative potentials and decrease of ORR specific activity with increasing contamination of ruthenium. However, in contrast to gradual changes in H_{upd} features, ORR specific activity showed a drastic ~45% decrease already for 0.15ML Ru/Pt and, in general, a pseudo-exponential decay with increased ruthenium coverage.

With the use of our DFT studies and previously published experimental results [20], we showed that the negative effect of ruthenium on ORR could be attributed to the masking of platinum sites by adsorbed ruthenium atoms, as well as to the oxophilic nature of ruthenium, that was found to bind O and OH much more strongly than platinum, reducing its effectiveness in ORR catalysis. Potentially unfavorable configuration of O_2 adsorption on platinum sites that immediately surround the ruthenium-masked platinum sites, the formation of bilayer islands and three-dimensional clusters and overlap between the deactivated platinum sites were proposed as a possible explanation for the exponential-like decay of ORR on ruthenium-contaminated catalysts.

The results of this research stress the negative impact of ruthenium dissolution from the anode and its crossover to the cathode in reformat-based PEMFCs and DMFCs. The dramatic reduction in ORR activity - almost 50% - and the subsequent reduction in power density that accompanied the smallest ruthenium contamination, emphasizes the need for development of PtRu catalysts with higher stability, Ru-pre-leaching procedures during catalyst/GDE/MEA preparation and control of anode potential during FC operation in order to avoid or at least to reduce the performance penalty caused by ruthenium crossover.

Acknowledgements

DK and EP wish to thank the Pazy Foundation for financial support for this research (Grant No. 289/2017). AN would like to thank the Planning & Budgeting Committee of the Council of High Education and the Prime Minister Office of Israel, in the framework of the INREP project.

References:

-
- ¹ S. Gottesfeld, T. A. Zawodzinski, Polymer Electrolyte Fuel Cells. In: Alkire RC, Kolb DM (eds) *Advances in Electrochemical Science and Engineering*, vol 5. Wiley-VCH, Weinheim, pp 195–301 (1997).
 - ² R. Borup, J. Meyers, B. Pivovar, Y. S. Kim, R. Mukundan, N. Garland, D. Myers, M. Wilson, F. Garzon, D. Wood, P. Zelenay, K. More, K. Stroh, T. A. Zawodzinski, J. Boncella, J. E. McGrath, M. Inaba, K. Miyatake, M. Hori, K. Ota, Z. Ogumi, S. Miyata, A. Nishikata, Z. Siroma, Y. Uchimoto, K. Yasuda, K. I. Kimijima, N. Iwashita, *Chem Rev.* **107**, 3904–3951 (2007).
 - ³ K. Shah, R.S. Besser, *Journal of Power Sources* **166**, 177–193 (2007).
 - ⁴ R. C. Urian, A. F. Gulla, and S. Mukerjee, *J. Electroanal. Chem.* **307**, 554–555 (2003)
 - ⁵ A. Pozio, R. F. Silva, M. De Francesco, F. Cardellini, L. Giorgi, *Electrochim. Acta*, **48**, 1625 (2003).
 - ⁶ M. Watanabe, S. Motoo, *J. Electroanalytical Chemistry and Interfacial Electrochemistry* **60**, 267–273 (1975).
 - ⁷ M. Watanabe, S. Motoo, *J. Electroanalytical Chemistry and Interfacial Electrochemistry* **60**, 275–283 (1975).

-
- ⁸ E. Antolini, *J. Solid State Electrochem.*, **15**(3) 455–472 (2010).
- ⁹ P. Jovanovič, V. S. Šelih, Martin Šala, S. Hočevar, F. Ruiz-Zepeda, N. Hodnik, M. Bele, M. Gaberšček, *Electrochimica Acta*, **211**, 851–859 (2016).
- ¹⁰ L. Gancs, N. Hakim, B. N. Hult, and S. Mukerjee, *ECS Transactions*, **3** (1), 607-618 (2006)
- ¹¹ N. Cabello - Morenoa, E. M. Crabb, J. M. Fisher, A. E. Russell, D. Thompsett, *ECS Transactions*, **16**(2), 483–496 (2008).
- ¹² P. Piela, C. Eickes, E. Brosha, F. Garzon, P. Zelenay. *J. Electrochem. Soc.*, **151**(12), A2053 (2004).
- ¹³ A. Schoekel, J. Melke, M. Bruns, K. Wippermann, F. Kuppler, C. Roth, *Journal of Power Sources* **301**, 210-218 (2016)
- ¹⁴ N.A. Anastasijević, Z.M. Dimitrijević, R.R.Adzic, *Electrochimica Acta*, **31**(9), 1125–1130 (1986).
- ¹⁵ M. Metikoš-Huković, R. Babić, F. Jović, Z. Grubač, *Electrochimica Acta*, **51**(7), 1157–1164 (2006).
- ¹⁶ D. Cao, A. Wieckowski, J. Inukai, N. Alonso-Vante, *J. Electrochem. Soc.*, **153**(5), A869 –A874 (2006).
- ¹⁷ V. Stamenkovic, B. N. Grgur, P. N. Ross, and N. M. Markovic, *J. Electrochem. Soc.*, **152**(2), A277–A282 (2005).
- ¹⁸ D. Kaplan, M. Goor, M. Alon, S. Tsizin, L. Burstein, Y. Rosenberg, I. Popov, E. Peled. *J Power Sources* **306**, 219–225 (2016).
- ¹⁹ L. Yang, M. B. Vukmirovic, D. Su, K. Sasaki, J. A. Herron, M. Mavrikakis, S. Liao, R. R. Adzic, *J. Phys. Chem. C* **117**, 1748–1753 (2013).
- ²⁰ L. Gancs, B. N. Hult, N. Hakim, S. Mukerjee, *Electrochem. Solid-State Lett.* **10**, 9, B150 (2007).
- ²¹ J. K. Nørskov, J. Rossmeisl, A. Logadottir, and L. Lindqvist, J. R. Kitchin, T. Bligaard, H. Jonsson, *J. Phys. Chem. B* **108**, 17886–17892 (2004).
- ²² L. Clare, A. Kucernak, *J. Phys. Chem. B* **106**, 1036 (2002).
- ²³ D. Kaplan, L. Burstein, I. Popov, E. Peled, *Journal of The Electrochemical Society*, **163** (9) F1004–F1010 (2016).
- ²⁴ K. Shinozaki, J. W. Zack, R. M. Richards, B. S. Pivovar, S. S. Kocha, *Journal of The Electrochemical Society* **162** (10) F1144–F1158 (2015).
- ²⁵ N. Hodnik, P. Jovanovič, A. Pavlišič, B. Jozinović, M. Zorko, M. Bele, V. S. Šelih, M. Šala, S. Hočevar, M. Gaberšček, *J. Phys. Chem. C* **119**, 10140–10147 (2015).
- ²⁶ H. A. Gasteiger, N. Markovic, P. N. Ross, Jr E. J. Cairns, *J. Phys. Chem.* **97**, 12020 (1993).
- ²⁷ I. Takahashi, S. S. Kocha, *Journal of Power Sources* **195**, 6312–6322 (2010).
- ²⁸ Y. Garsany, I.L. Singer, K.E. Swider-Lyons, *Journal of Electroanalytical Chemistry* **662**(2), 396 – 406 (2011).
- ²⁹ K. Shinozaki, J.W. Zack, S. Pylypenko, B.S. Pivovar, S.S. Kocha, *Journal of The Electrochemical Society* **162**(12), F1384–F1396 (2015).
- ³⁰ F. Nart, W. Vielstich, *Handbook of Fuel Cells - Fundamentals, Technology and Applications*, Ch. 21, Vol. 2, edited by W. Vielstich, H. A. Gasteiger, A. Lamm, John Wiley & Sons, Ltd (2010).
- ³¹ S. S. Kocha, Y. Garsany, D. Myers (2013) Testing Oxygen Reduction Reaction Activity with the Rotating Disc Electrode Technique DOE webinar energy.gov/eere/fuelcells/webinar-testing-oxygen-reduction-reaction-activity-rotating-disc-electrode-technique,

http://energy.gov/sites/prod/files/2014/03/f12/webinarslides_rde_technique_031213.pdf, accessed at 12/05/2020

- ³² D. Kaplan, L. Burstein, I. Popov, E. Peled, *Journal of The Electrochemical Society*, **163**(9) F1004-F1010 (2016).
- ³³ D. Kaplan, M. Goor, L. Burstein, I. Popov, M. Shviro, E. Peled. *Journal of Solid State Electrochemistry* **24**, 2385–2393 (2020).
- ³⁴ D. Durst, C. Simon, F. Hasché, H.A. Gasteiger, *Journal of The Electrochemical Society* **162**(1), F190-F203 (2015).
- ³⁵ P. E. Blöchl, Projector augmented-wave method. *Phys Rev. B* **50**(24), 17953–17979 (1994).
- ³⁶ G. Kresse, G. Joubert, *Phys Rev B - Condens Matter Mater Phys* **59**(3), 1758–1775 (1999).
- ³⁷ G. Kresse, J. Furthmüller, *Phys. Rev. B* **54**(16), 11169–11186 (1996).
- ³⁸ H. Jürgen, *J. Comput Chem* **29**, 2044–2078 (2008).
- ³⁹ C. E. Calderon, J. J. Plata, C. Toher, C. Oses, Ohad Levy, M. Fornari, A. Natan, M. J. Mehl, G. Hart, M. B. Nardelli, S. Curtarolo, *Comp. Mat. Sci.* **108**, 233–238 (2015).
- ⁴⁰ J. L. F. Da Silva, C. Stampfl, M. Scheffler, *Surf. Sci.* **600**, 703–715 (2006).
- ⁴¹ P. Haas, F. Tran, P. Blaha, *Phys. Rev. B* **79**, 085104 (2009).
- ⁴² W. Davey, *Phys. Rev.* **25** (6), 753–761 (1925).
- ⁴³ C. Kittel, *Introduction to Solid State Physics*, 7th ed.; John Wiley & Sons: New York, 1996
- ⁴⁴ C. Stampfl, M. Scheffler. *Phys. Rev. B* **54** (4), 2868 (1996).
- ⁴⁵ *Physics of Solid Surfaces: Electronic and Vibrational Properties*, edited by G. Chiarotti, Landolt-Bornstein, New Series, Group III, Vol. 24, Pt. Springer-Verlag, Berlin, 1994.
- ⁴⁶ K. Mathew, R. Sundararaman, K. Letchworth-Weaver, T. A. Arias, and R. G. Hennig, *J. Chem. Phys.* **140**, 084106 (2014).
- ⁴⁷ K. Mathew, V. S. C. Kolluru, S. Mula, S. N. Steinmann, R. G. Hennig. *J. Chem. Phys.* **151**, 234101 (2019).
- ⁴⁸ J. K. Nørskov, T. Bligaard, A. Logadottir, S. R. Bahn, L. B. Hansen, M. V. Bollinger, H. S. Bengaard, B. Hammer, Z. Sljivancanin, M. Mavrikakis, Y. Xu, S. Dahl, C. J. H. Jacobsen, *J. Catal.* **209**, 275 (2002).
- ⁴⁹ Q. Deng, J. Zhao, T. Wu, G. Chen, H. A. Hansen, T. Vegge. *Journal of Catalysis* **370**, 378–384 (2019)
- ⁵⁰ T. T. H. Cheng, N. Jia, P. He, *Journal of The Electrochemical Society* **157**(5), B714–B718 (2010).
- ⁵¹ J.P. Zheng, P.J. Cygan, T.R. Jow, *Journal of The Electrochemical Society* **142**(8), 2699–2703 (1995).
- ⁵² F. Richarz, B. Wohlmann, U. Vogel, H. Hoffschulz, K. Wandelt, *Surface Science* **335**, 361–371 (1995).
- ⁵³ W. R. Tyson, W.A. Miller, *Surface Science* **62**, 267–276 (1977).
- ⁵⁴ L. Vitos, A. V. Ruba, H. L. Skriver, J. Kollar, *Surface Science* **411**, 186–202 (1998).
- ⁵⁵ N. E. Singh-Miller, N. Marzari, *Phys. Rev. B* **80**, 235407 (2009).
- ⁵⁶ W. F. Lin, M. S. Zei, M. Eiswirth, G. Ertl, T. Iwasita, W. Vielstich, *J. Phys. Chem. B* **103**, 6968–6977 (1999).

-
- ⁵⁷ J. S. Spendelow, P.K. Babu, A. Wieckowski, *Current Opinion in Solid State and Materials Science* **9**, 37–48 (2005)
- ⁵⁸ Z. Gu and P. B. Balbuena, *J. Phys. Chem. C* **111**, 9877–9883 (2007).
- ⁵⁹ A. Kokalj, A. Lesar, M. Hodosecek, M. Causa, *J. Phys. Chem. B* **103**, 7222–7232 (1999).
- ⁶⁰ D. C. Ford, Y. Xu, M. Mavrikakis, *Surface Science* **587**, 159–174 (2005).
- ⁶¹ J. A. Herron, S. Tonelli, M. Mavrikakis, *Surface Science* **614**, 64–74 (2013).
- ⁶² G. Henkelman, A. Arnaldsson, H. Jónsson, *Comput. Mater. Sci.* **36**, 354–360 (2006).
- ⁶³ E. Sanville, S. D. Kenny, R. Smith, G. Henkelman, *J. Comp. Chem.* **28**, 899–908 (2007).
- ⁶⁴ L. Yang, M. B. Vukmirovic, D. Su, K. Sasaki, J. A. Herron, M. Mavrikakis, S. Liao, R. R. Adzic, *J. Phys. Chem. C* **117**, 1748–1753 (2013).
- ⁶⁵ T. Bligaard, J. K. Nørskov, *Electrochimica Acta* **52**, 5512–5516 (2007).
- ⁶⁶ R. R. Adzic, *Electrocatalysis (Frontiers in Electrochemistry)*, p 197 edited by J. Lipkowski, P. N. Ross, Wiley-VCH: New York (1998).
- ⁶⁷ A. U. Nilekar, M. Mavrikakis, *Surf. Sci.*, **602**, L89–L84 (2008).
- ⁶⁸ C. F. Zinola, A. J. Arvia, G.L. Estiu, E. A. Castro, *J. Phys. Chem.*, **98**, 7566–7576 (1994).
- ⁶⁹ E. Leiva, C. Sánchez, *Handbook of Fuel Cells - Fundamentals, Technology and Applications*, Ch. 11, Vol. 2, edited by W. Vielstich, H. A. Gasteiger, A. Lamm, John Wiley & Sons, Ltd (2010).
- ⁷⁰ N. Cabello - Moreno, E. M. Crabb, J. M. Fisher, A. E. Russell, D. Thompsett, *ECS Transactions*, **16** (2) 483–496 (2008)
- ⁷¹ J.-Y. Park, M. A. Scibioh, S.-K. Kim, H.-J. Kim, I.-H. Oh, T. G. Lee, H. Y. Ha, *Int. J. Hydrogen Energy*, **34**, 2043 – 2051 (2009)
- ⁷² J.-Y. Park, J.-H. Kim, Y. Seo, D.-J. Yu, H. Cho, S. J. Bae, *Fuel Cells* **12**, (3), 426–438 (2012)
- ⁷³ J.-Y. Park, J.-H. Lee, J. Sauk, I.-H. Son, *Int. J. Hydrogen Energy*, **33**, 4833–4843 (2008)